Measurement of Three Dimensional Volcanic Plume Properties using Multiple Ground Based Infrared Cameras

Kieran Wood[a], Helen Thomas[c], Matt Watson[c], Andrew Calway[b], Tom Richardson[a], Kerstin Stebel[d], Ailsa Naismith[c], Lucy Berthoud[a], Josh Lucas[c]

[a]*Department of Aerospace Engineering, University of Bristol, BS8 1TR, UK*
[b]*Department of Computer Science, University of Bristol, BS8 1UB, UK*
[c]*School of Earth Sciences, University of Bristol, BS8 1RJ, UK*
[d]*NILU – Norwegian Institute for Air Research, NO-2027 Kjeller, Norway*

Abstract

This study presents a method and a proof of principle system for the direct measurement of volcanic plume 3-D spatial properties. The shape of a plume is reconstructed in three dimensions using multi-view imagery collected from static ground-based cameras. The method was developed using data collected during an expedition to Volcán de Fuego in Guatemala, where four thermal infrared cameras were deployed to capture simultaneous images of the regular ash-rich eruptions. A space carving method was applied to the problem to estimate the volume of the plume at any moment in time. By successively applying the method to sequential sets of images, other quantitative measurements such as the drift direction, ascent rate, and dispersion rate can be deduced. The complete method work-flow is presented including data capture, calibration processes, image processing, the space-carving method, and practical implementation issues. The method is sensitive to the camera alignment, hence a novel technique for estimating the camera orientation angles, making use if a high-accuracy terrain model, is described. Other sources of error relating to the number, synchronisation and resolution of the cameras are also discussed. Preliminary results are presented using data collected at Volcán de Fuego in November 2017 over a period of 1.25 h including three distinct eruptions.

Keywords: 3D reconstruction, volcano, plume, thermal, space carving, computer vision

1. Introduction

Volcanoes are point source emitters of a range of gases and ash, and, via both explosive and effusive activity, transfer significant amounts of material from the lithosphere to the atmosphere. The emitted species contained within volcanic plumes carry information about subsurface processes [1], are harmful to the proximal environment [2], including human populations [3], and, even at distances greater than 1000 km, ash can be hazardous to civil and military aircraft. Within civil aviation, between 1953 and 2014 there have been 221 reported encounters, with two of them deemed to be class 4; loss of power to all engines [4, 5].

Global airspace is currently managed using a combination of satellite imagery, providing a 2-D snapshot [6], and dispersion modelling, providing a 3-D prediction based on a priori information of the ash cloud's position and content. Satellite data can be used, with many assumptions and under ideal meteorological conditions, to

retrieve optical depth, effective radius and, by extension, column integrated mass [7]. Such data can also be used to drive dispersion models through data insertion techniques [8, 9], but in general, models and observations are typically only used in concert for validation and sensitivity analysis [10]. Source terms for models are often poorly constrained and can lead to significant downstream uncertainties [11, 12]. From a volcanological perspective ground-based imaging has become a commonly used technique for determination of sulphur dioxide (SO_2) and ash emission rates using both ultraviolet (UV) and infrared (IR) technologies [13, 14, 15].

Since the eruption of Eyjafjallajökull in 2010 [16] there has been a change in airspace management policy from a zero tolerance (avoid all ash) approach to a threshold-based policy [17]. This threshold is based upon a 'safe-to-fly' concentration ($2\,\mathrm{mg\,m^{-3}}$) above which civil aviation are unable to fly without a safety case, and never above $4\,\mathrm{mg\,m^{-3}}$. The severity of harm to a jet engine is best determined by dose, which is a measure combining the concentration and exposure duration. 2-D observations from both ground-based and satellite-based platforms cannot measure true concentration or dose. Nor can they model the cloud in three dimensions, a critical piece of information of use to airspace managers. Forward-looking, aircraft mounted instruments capable of measuring ash burden ahead of the aircraft path could be used to infer dosage, although the development of such instruments are still in their infancy [18]. Presently, dose can only be estimated operationally based on dispersion model outputs, which therefore are subject to any inherent uncertainty of the chosen model [19].

It has been suggested that the use of several, multispectral IR cameras could be utilised to retrieve the 3-D structure of volcanic plumes [20, 21, 22]. This paper details a prototype system for mapping the shape of volcanic ash plumes in three dimensions using simultaneous IR imagery captured from multiple ground viewpoints. Referring to Figure 3, a process of space carving is implemented whereby a discretised search region (the sky above the volcano) is systematically classified by assessing the plume visibility in multiple segmented 2-D images. The following sections explain the work-flow shown in Figure 1. Details of the input data-set are given in section 3. Although the method was developed based upon case-study data-set captured at Volcán de Fuego in Guatemala, in principal it can be applied more generally to other plumes and other camera systems. Essential mathematical transformations and calibrations are discussed in sections 4.2 and 4.3. The 2-D image segmentation is explained in section 4.4, and the overall 3-D reconstruction method in section 4.1. Finally, the time-series data is processed to extract higher-level information with the results and discussion in Section 5.

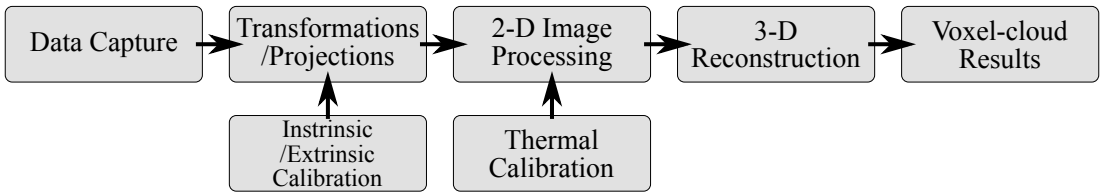

Figure 1: An overview of the plume reconstruction processing work-flow.

2. Related Work

Remote sensing of volcanic plumes is a commonly used technique in the field of volcanology. Since the 1970's instruments have targeted several spectroscopic regions to derive emission rates, typically, though not exclusively, targeting sulphur dioxide due to its high signal (the third most abundant volcanic gas) to noise (very low ambient concentrations) ratio. Almost all techniques used today integrate, out of necessity, over line-of-sight. These include both scanning Differential Optical Absorption Spectroscopy (DOAS) [23] and imaging techniques [24], [14]. This has two important ramifications if concentrations, rather than emission are to be retrieved: (1) an estimate of the third dimension is required, which often introduces significant error and (2) only an average concentration along the line of sight can be derived. Recent works have cited the need for, and theoretically described, 3-D tomographic techniques [25, 26]. Similar 3-D retrievals have also been proposed using networks of small satellite systems [27]. Furthermore, computer vision and image processing techniques that have already been applied in 2-D [28, 22, 29, 30] can be applied in 3-D to yield information regarding plume dynamics such as turbulence.

The use of Structure from Motion (SfM) methods has become increasingly popular due to the availability of commercial software packages with flexible implementations. Such applications have been used to estimate the Cloud Top Height (CTH) using images captured from space [27] and to estimate a snapshot 3-D plume shape using images captured from a unmanned aerial vehicle [31]. In both cases the multi-view images were captured sequentially, hence made assumptions on the slow evolution of the scene compared with the capture duration. In this study, multiple cameras were deployed to capture simultaneous images therefore avoiding issues caused by a changing scene.

This work is an important step towards measuring the *internal* structure of a plume to better understand the quantity of ash entering the atmosphere and its distribution. Under ideal circumstances, Computed Tomography (CT) methods [32] could be applied since there are similarities between the attenuation of an X-ray passing through organic tissue and the integral burden measurement from IR cameras observing a gas plume; both are indistinguishably affected by the path-length and the density of the material along that line, hence acting as integral measurements. When considering the general CT problem, a greater number of cameras allows a greater amount of internal structure to be resolved. Medical CT scanners capture images from hundreds of directions allowing the differentiation of internal features differing in density by 1%. However, the difficulty of distributing large numbers of cameras around a volcano severely limits the application of established tomography methods. For limited view points, the discrete tomography methods seem more appropriate [33], but only recover binary structures and have significant errors. In other work, the 2-D internal SO_2 concentration distribution was measured by using airborne traverse technique using three UV spectrometers [34] . Analytical models have been utilised alongside broadband thermal infrared imagery to reconstruct the ash concentration and size distribution in 2-D [35].

Three-dimensional vision methods have been applied in a range of non-volcanic scenarios. The ellipsoid shape of rising bubbles was measured using stereo-cameras [36]. A stereo computer vision method was implemented to track meteorological clouds in 3-D using ground based cameras. Quantitative metrics, such as the cloud-base height, were estimated [37, 38]. The 3-D shape of an industrial plume was

measured using scanning imaging IR spectroscopy sensors from two view points [39].

3. Data Collection

A multi-view image data set was collected at Volcán de Fuego in Guatemala (14.474 702°N, 90.880 861°W) during an expedition in November 2017. Fuego is an active stratovolcano and it provides an ideal target for plume reconstruction because it is (1) predictably active [40, 41], with small ash bearing explosions with a repose period of <1 h, (2) accessible by road from a distance of < 15 km from a number of observation azimuths and (3) at a high enough altitude (summit 3763 AMSL), with observation points between 1130 - 1470 AMSL which reduce atmospheric contamination effects. The acquisition was made during clear meteorological conditions from four sites within 12 km of the summit. Meteorological clouds are opaque in the infrared and prevent the ash cloud from being detected which provides a fundamental limitation to the continuous operation of the system. The measured GPS locations of the cameras are given in Table 1 and displayed in Figure 2(c).

The data set was recorded on the morning of 2018-11-07 starting at approximately 06:00 UTC. The filter-wheel based cameras were set to their maximum capture rate which resulted in approximately 7 frames per minute (see Figure 9). The four camera system was run for a duration of approximately 1.25 h recording a minimum of 350 images per camera. During this time three distinct eruptions occurred, and although not at a scale where aviation would be affected, the observed explosions are of a sufficient size to develop and test algorithms.

Name	Lat. φ (°)	Lon. λ (°)	Azimuth ψ (°)	Elevation θ (°)	Dist. (km)
SMD	14.516129	-90.805053	243.0	15.2	11.5
LAZ	14.428491	-90.833062	314.0	19.5	7.2
OBS	14.432332	-90.935826	49.0	20.0	7.6
YEP	14.501396	-90.952078	112	15.0	8.4

Table 1: Locations and orientation of each of the four camera systems: SMD, LAZ, OBS and YEP. The azimuth (the horizontal angular distance relative to North) and elevation (the vertical angular distance relative to the local plane) angles were measured in the field using a basic compass and inclinometer. The distance is relative to the summit of Fuego.

3.1. IR Cameras

Four similar NicAIR infrared camera systems were used (see Figure 2(d)). Each system consists of a FLIR Photon 640 camera core with a 644 × 512 pixel microbolometer array and sensitivity in the thermal infrared (7.5 µm - 13.5 µm). The cameras were equipped with 25 or 35 nm Germanium lenses. The filter wheel in front contained up to four narrow bandpass (≈ 1 µm full width half max) filters. The camera is calibrated in the laboratory using a black-body source. It also contains a black-body shutter, which is placed in the field of view before each scene view to provide an in field temperature calibration. The ability to acquire multispectral data across narrowband channels allows for the estimation of SO_2 and ash mass loading [21, 20]. Despite a reduction in spatial resolution compared to optical cameras, IR cameras were used as (a) they provide night-time images when meteorological clouds

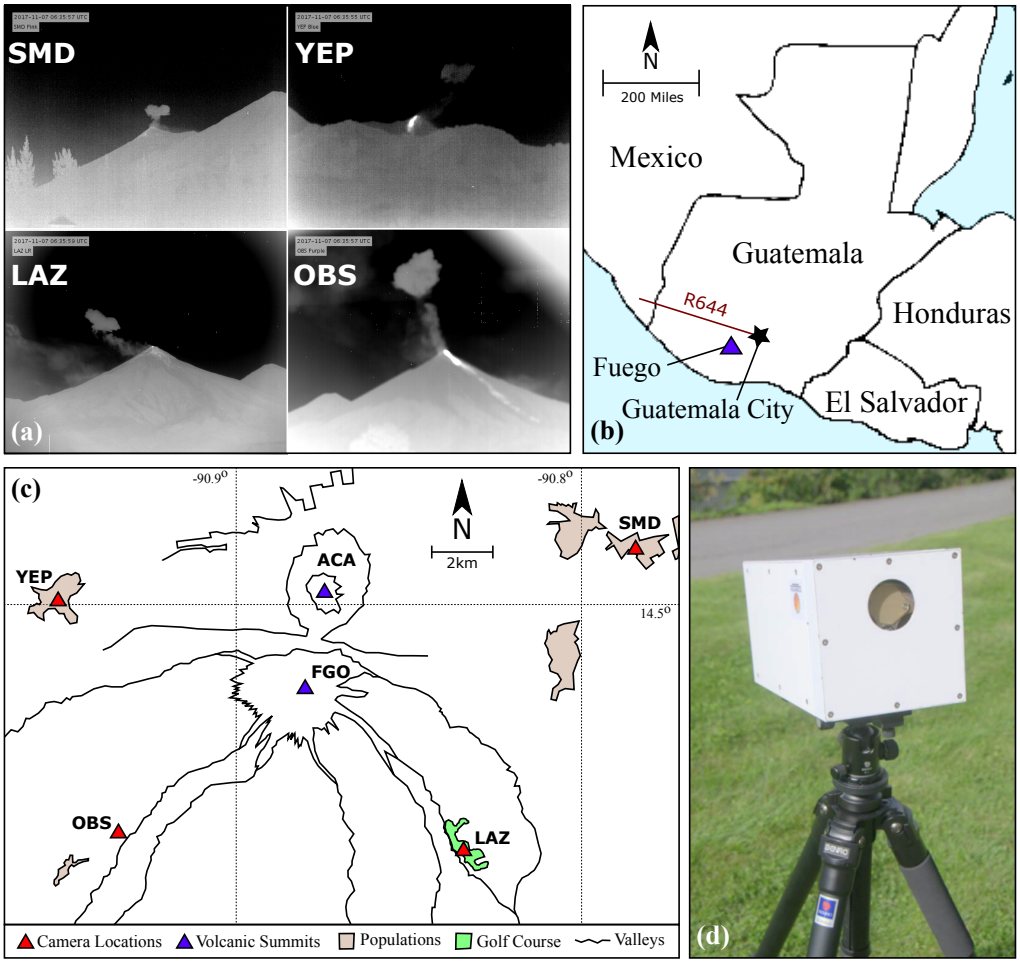

Figure 2: (a) Example broadband thermal images shortly after an eruption with the plume visible above the summit. (b) The region of operation within 40 km of Guatemala City airport and near the often closed R644 airway. (c) The arrangement of the cameras during the November 2017 campaign. The summit vent is denoted by FGO. Major population centres are also shown. (d) The NicAIR multi-spectral IR camera.

clear and (b) the possibility, in future work, to retrieve 3-D ash concentrations from images of 2D ash mass loading (integrated over line-of-sight). Although this study focuses on IR cameras, the algorithm could be applied to any multi-view image set where the plume can be easily differentiated from the ground or background sky, hence visible cameras might be used to reduce complexity and cost.

To retrieve temperature data, and from that ash mass, a thermal calibration process is required. However, since the segmentation of plume pixels can be achieved using uncalibrated images, this is not considered here. The segmentation algorithm is based on the strong brightness temperature difference between the ash cloud and the clear sky background (see Section 4.4), which allows plume pixels to be identified using a difference threshold. This works well for the diluted plumes considered in the study, however for much larger plumes which might reach the stratosphere and therefore cool significantly, a more sophisticated method of differentiating the plume from the background might be required. For example using brightness temperature difference images (10 µm - 12 µm) would enable to retrieve volcanic ash particle size, mass and optical depth from the thermal infrared camera [20].

3.2. Camera Synchronisation

Each camera was linked to a control PC running control software supplied by researchers at the Norwegian Institute for Air Research (NILU). The software allowed the automatic capture of image sequences at a user defined rate. For each capture sequence, the camera saves the raw IR count data into a sequentially named file with accompanying time and shutter temperature as meta-data. The capture time was accurate to the nearest second and set from the PC clock. All control PC clocks were synchronised at the start of the experiment and had negligible drift over the duration of the 1.5 h data collection, however the interval between capture sequences varied due to differences between the control PCs processing power. Ideally, a high accuracy and absolute clock, such as GPS time, would be used to simultaneously trigger the cameras at defined times referenced to a shared absolute datum time, however the supplied software was not capable of this function. The camera also periodically captures a calibration image of the closed lens shutter, allowing for a correction in the temperature drift. An example of simultaneously captured images from the four cameras is shown in Figure 2(a), with the plume visible after a recent explosion.

3.3. Digital Elevation Model

A Digital Elevation Model (DEM) was utilised for part of the camera calibration process (Section 4.3). This DEM was derived from TanDEM-X 12 m resolution data which was obtained thanks to the German Aerospace Center (DLR Proposal ID 1552 - PI Christelle Wauthier, The Pennsylvania State University). The DEM covers an area 14 km by 14 km with the volcanic summit located at the centre. The resolution is $1.1111 \times 10^{-4}\,^{\circ}\,\mathrm{px}^{-1}$, which equates to approximately $12.3\,\mathrm{m\,px}^{-1}$. The locations and altitudes are expressed in the WGS84 reference system. A rendered image of the DEM is shown in figure 4(a).

3.4. Coordinate Transformations

The space carving method adopted is defined within a orthogonal Cartesian coordinate system, hence the process described by [42, chap. 2] is used to convert locations expressed in the WGS84 reference system (latitude, longitude, and altitude) into a right hand North, East, Down (NED) system. This is an exact transformation and incorporates the curvature of the Earth. Details are provided in Appendix B.

4. Multiview 3-D Ash Plume Reconstruction

This section sets out the details of the space carving method for estimating the 3-D volume of the ash plume based on the image sequences captured from the ground based cameras. It begins with an overview of the core algorithm, followed by details of the individual components and practical implementation. Results based on the data captured for the Volcán de Fuego are then presented in Section 5.

4.1. Space Carving

Figure 3 provides an illustration of the space carving method using images captured from the four ground based cameras situated around the base of the volcano. Space carving has been used extensively for 3-D reconstruction in computer vision

[43]. A simplified version of the method was adopted in this work in order to provide a 'proof of concept' system. The 3-D space above the volcano is represented in terms of a regular volumetric grid consisting of voxels, with the size of the latter determining the resolution of the representation. Each voxel is considered in turn and the pixel values corresponding to its projection into each of the four cameras determines its classification as either a plume or a free-space voxel. The classification is based on segmentation of the ash plume in each image using a grey level threshold technique and the constraint that the projections in all four cameras should correspond to an ash plume pixel. The latter follows from the assumption that the plume volume of interest is visible in all the cameras and is not occluded by foreground objects.

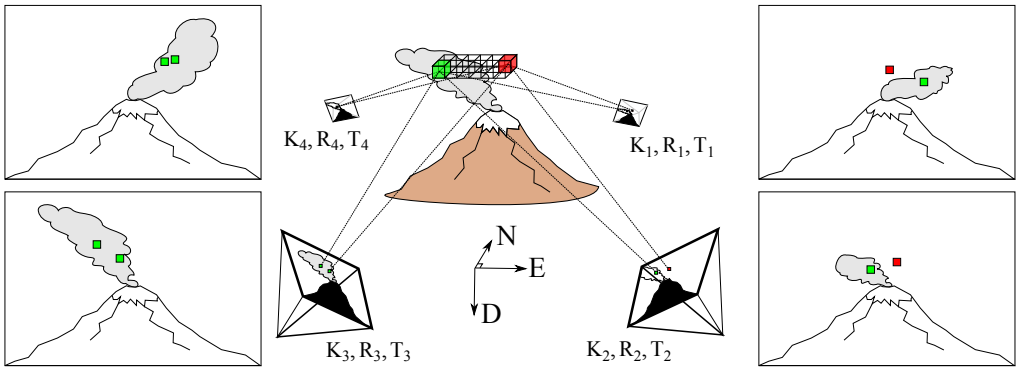

Figure 3: A diagram representing the method of space carving. A region of 3-D space (voxel) is projected into the 2-D image (pixel) planes of cameras surrounding the plume. If pixel location is within the plume for all cameras, then the voxel is retained (green). If the pixel location is outside of the plume for one or more cameras, the voxel is discounted (red). The process is systematically repeated over a search volume, until only the voxels identified as plume remain.

To formalise the above, let $\mathbf{V}$ denote the centre of a voxel within the volumetric grid with resolution δ_v, and let $\mathbf{v}_k$ denote its projection into the kth ground camera. Assuming a perspective projection model in 3-D Cartesian space and using homogeneous coordinates, these are related as follows [44]:

$$\mathbf{v}_k = \begin{bmatrix} v_{kx} \\ v_{ky} \\ 1 \end{bmatrix} \cong \mathbf{K}_k \mathbf{R}_k \left[\mathbf{I}\right| - \mathbf{T}_k] \, \mathbf{V} = \mathbf{K}_k \mathbf{R}_k \left[\mathbf{I}\right| - \mathbf{T}_k] \begin{bmatrix} V_x \\ V_y \\ V_z \\ 1 \end{bmatrix} \tag{1}$$

where $\mathbf{I}$ denotes the 3×3 identity matrix and for the kth camera, $\mathbf{K}_k$ denotes the 3×3 camera matrix encoding its intrinsic parameters and $\mathbf{R}_k$ and $\mathbf{T}_k$ denote the 3×3 rotation matrix and 3×1 translation vector defining its orientation and position with respect to a world coordinate system, respectively. The voxel projection into the kth camera is then defined by the pixel location (v_{kx}, v_{ky}). Classification of each voxel is then defined as follows:

$$C(V) = \begin{cases} 1 & \text{if } \; S_k(v_{kx}, v_{ky}) = 1 \;\; \forall \;\; k \\ 0 & \text{otherwise} \end{cases} \tag{2}$$

where $C(V) = 1$ if V is within the plume and $C(V) = 0$ if it is in free space. $S_k(x, y)$ is the plume segmentation of the kth camera image such that $S_k(x, y) = 1$ if pixel (x, y) corresponds to the plume and $S_k(x, y) = 0$ otherwise.

Implementation of the above algorithm requires calibration of the cameras to determine the camera matrices $\mathbf{K}_k$, estimation of the position $\mathbf{T}_k$ and orientation $\mathbf{R}_k$ of each camera, and generation of the plume segmentation images $S_k(x, y)$. These components are described in the following sections.

4.2. Estimation of Camera Matrix

The camera intrinsic matrix describes the physical camera properties, such as the pixel sizes, and also the optical properties, such as the focal length. For this work, a simple camera model has been used and is defined as,

$$\mathbf{K} = \begin{bmatrix} f & s & c_x \\ 0 & \alpha f & c_y \\ 0 & 0 & 1 \end{bmatrix} \tag{3}$$

where f is the focal length, α is the pixel aspect ratio, s is the pixel skew, and $[c_x, c_y]$ defines the principal point. For the purposes of this study it has been assumed that the sensor pixels are both perfectly square, $\alpha = 1$, and that they are regularly aligned on an orthogonal grid ($s = 0$).

The focal length and principal point can be found from the data sheets for the thermal cameras, however the addition of the narrow band filters potentially introduces optical disturbances. Only two cameras were available for calibration (one fitted with a 25 mm lens and one fitted with a 35 mm lens) and the process used the technique described by [45]. This involved capturing images of a chequerboard calibration target from multiple view points. A custom thermal target was created such that the chequerboard pattern is clearly visible in the thermal spectrum. A full explanation of the hardware and the calibration results are given in Appendix A. The estimated parameters for focal length and principal point closely matched those given on the data sheet and thus data sheet values were used for the other two cameras which were unavailable for precise calibration.

A lens model was not included in the projection process, however this was acceptable since the plume mostly occupied the centre of the images where the effect of lens distortion are minimal. The camera calibration process also estimated the lens distortion coefficients and these could be incorporated in the future.

4.3. Estimation of Camera Position and Orientation

The camera positions $\mathbf{T}_k$ with respect to a world coordinate system were estimated from GPS measurements captured at installation. Longitude (ψ_k) and latitude (φ_k) values were converted into local Euclidean coordinates using the algorithm described in [42] and summarised in Appendix B, with the altitude provided by interpolation from the DEM. Although GPS measurements from consumer grade smart-phone devices can suffer with errors of up to $\pm 4m$ [46], this is a small percentage ($< 0.06\%$) when compared to the distance between the volcano and the cameras as given in Table 1 and thus has marginal impact on the reconstruction results.

Initial estimates of the orientation of each camera were obtained at installation using basic compass and inclinometer measurements, giving azimuth (yaw) and elevation (pitch) values as also indicated in Table 1. The bank (roll) of each camera was assumed to be zero by ensuring that they were installed in a horizontal position based on spirit level measurements. The error in these measurements, however,

prove to be significant when considering projections from the large distances being considered. Thus improved estimates were obtained using an image alignment method based on the projection of the DEM into each camera. This is illustrated in Figure 4 and described below.

Correction of the three orientation measurements was based on the idea of aligning the observed outline of the volcano in the camera images (Figure 4(b)) with that obtained by projecting the outline obtained from the DEM into each camera view (Figure 4(c)). Estimation of the 3-D orientation for each camera was then iterated until a least squares cost was minimised. The DEM projection was performed at the same resolution as the real cameras, allowing a cost function to be defined using one-to-one comparison of pixels. Given the clarity of the division between the land and sky in both the real image and the rendered image, this cost function was defined based upon a comparison of the skyline of the volcano, giving a quantitative measure of how well the two images aligned. Considering the diagram in Figure 4(b), for the ith column of pixels in one of the images, the vertical pixel location, d_i, of the land-sky division was determined, creating a vector of pixel locations $\mathbf{D} = [d_1, d_2, ...d_i]$ for $i = 1 : N$, where N is the image width. Let $\mathbf{D}_{real}$ and $\mathbf{D}_{render}(\phi, \theta, \psi)$ denote these vectors for the captured and DEM rendered images, respectively, where the latter depends on the orientation triplet (ϕ, θ, ψ), representing the azimuth, elevation, and bank angles, respectively. $\mathbf{D}_{real}$ was created manually using a suitable frame from the captured image sequence and $\mathbf{D}_{render}(\phi, \theta, \psi)$ was created automatically at each iteration by projecting the DEM into the camera view using Equation 1 and the current estimates of the orientation triplet, along with the known camera position and intrinsic parameters. The cost is thus a function of the orientation triplet and computed as the squared difference between the two vectors, i.e. $C(\phi, \theta, \psi) = ||\mathbf{D}_{real} - \mathbf{D}_{render}(\phi, \theta, \psi)||^2$, where $||.||$ denotes vector length.

The measured azimuth, elevation and bank angles being used to initialise the optimisation. The underlying system model is not defined mathematically here because it utilised a simulated projection of the DEM using 3-D animation software. All camera position and DEM data was first transformed into a local Cartesian coordinate system before generating the artificial images. Since the software allowed for the background, or 'sky', colour to be set to an exact value (note the monochrome sky colour in Figure 4(d)), the automatic extraction of the outline was achieved by searching pixel intensity values in each column of the image until the first non-sky value was detected. The model gradient is therefore also not available *a priori* and will be calculated numerically during the estimation. Inequality constraints were added to ensure the optimisation only searched in a small region ($\pm 7)^\circ$) near the initial condition and did not diverge to false minimum solutions. This was acceptable due to the relative accuracy of the measured camera orientations, however an alternative approach could be to initialise the optimisation using orientations trigonometrically calculated by assuming the centre pixel of each camera was perfectly aimed at the volcanic summit. Given the reasons above, an implementation of the sequential quadratic programming (SQP) optimisation algorithm was used to minimise $C(\phi, \theta, \psi)$ since it converges quickly under circumstances where evaluation of the model and its derivatives is time-consuming.

The process was repeated for each of the four cameras, and convergence occurred after approximately one hundred iterations. Due to the interaction with the animation software at each step of the optimisation, the convergence time was on

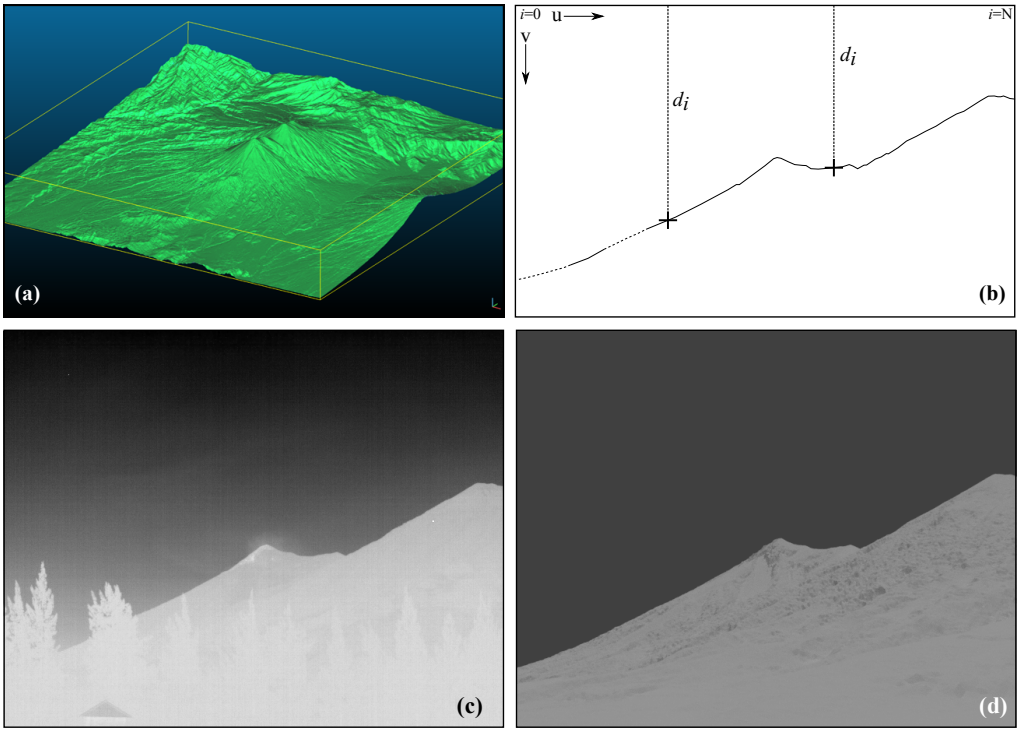

Figure 4: (a) The local DEM model, derived from Tandem X at a resolution of 12 m per pixel. A comparison of (c) a real image captured from the IR camera, and (d) the rendered image based upon the DEM. The cost function (b) is based-upon the RMS error between the vertical pixel locations of the two skylines.

the order of tens of minutes, however this was acceptable since the cameras were static and the orientations only needed to be optimised once. Note that the method assumes that there is sufficient clarity and variation in the volcano outline to facilitate unique alignment. Any time-varying features obstructions between the camera and the horizon, such as moving vegetation or flags etc., or self-repeating structures could lead to a false minimum. It is also assumed that the large scale features of the flanks of the volcano have remained constant between the date of the DEM data and the date of image capture, which was the case for the data used. Significant topographic changes (including earthquakes, landslides, and vegetation growth) would require an alternative approach.

4.4. Image Segmentation

The 2-D images captured from each camera were pre-processed using the four stages described below to identify the pixels within the plume and produce the binary arrays $S_k(x, y)$.

1. *Temperature drift normalisation.* To account for long-term temperature variations of the camera system, for example due to the camera cooling during the capture period, the temporally closest shutter calibration image is subtracted from the raw IR image (Figure 5(a)).
2. *Sky-Ground segmentation.* The sky is then segmented from the ground by applying a mask (Figure 5(b)). Since the cameras are static, the mask for each camera is constant and created manually.
3. *Temperature gradient removal.* The next stage removes the effect of the temperature gradient introduced by the lower atmosphere being hotter than the

high altitude atmosphere. For each camera an image was manually selected with the minimal plume visible. This was then subtracted from all of the images in the sequence. A secondary beneficial effect of this stage was to remove the image artefacts introduced by the Germanium glass window on the permanently mounted camera (LAZ). This can be seen introducing a vignette effect into Figure 5(b). Due to the removal of other factors, the only temperature differences seen in the image are due to the plume (Figure 5(c)).

4. *Plume segmentation.* The final stage is the application of a threshold filter, effectively making a binary image (Figure 5(d)) where the plume pixels are identified. Due to the distinctiveness of the eruptive plume, the threshold value was not critical and was set manually.

Given the small data set used in this study, the 2-D image processing described above was semi-automated. However, for permanent monitoring, some greater level of autonomy could be introduced using more advanced image segmentation algorithms.

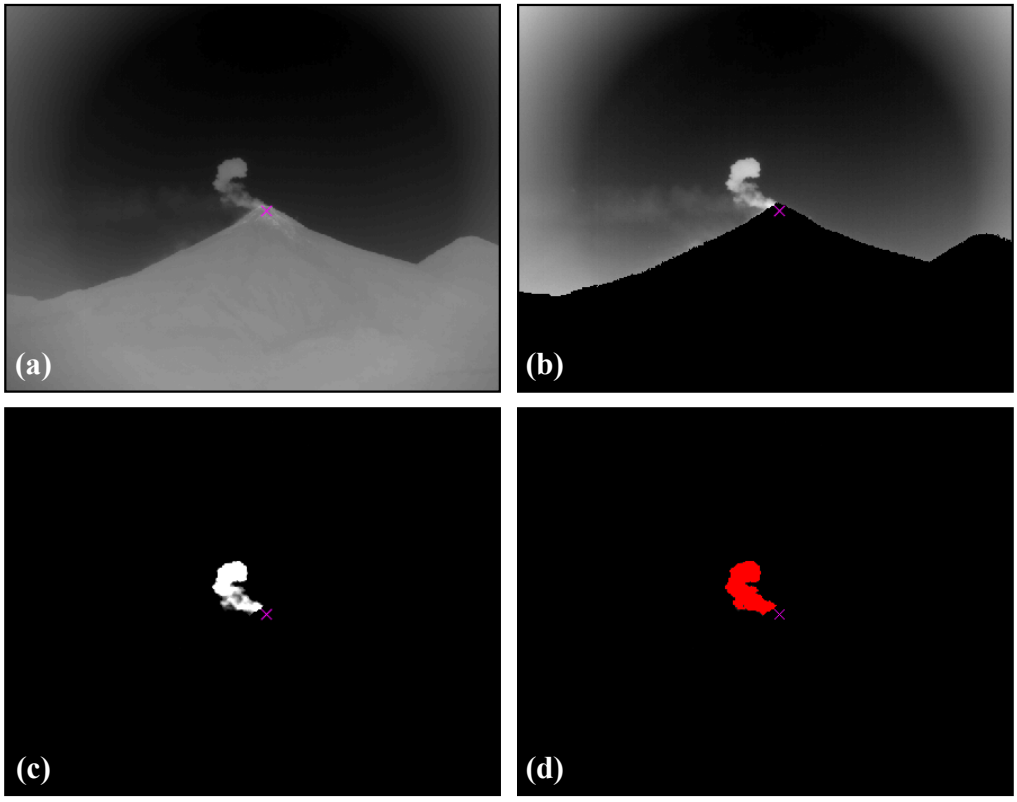

Figure 5: The four stages of 2-D image processing to identify the pixels within the plume: (a) temperature drift normalisation; (b) sky-ground segmentation; (c) temperature gradient normalisation; (d) plume segmentation - the red pixels indicate those meeting the threshold criteria.

4.5. Sequence Processing and Adaptive Search

The image segmentation and space carving processing steps were applied to quads of images which were aligned closest in time to a marching interval (t_s) over the entire capture time. At each processing step, the image set was checked to see if a new image had been captured. If so, the quad was updated with the new image; if not the most recent image captured remained in the quad. The variations in the capture interval on each camera (as seen in Figure 9) means at each step the camera

images can be up-to 9-11s old. To give an indication of this effect, the cumulative age of the images at each processing step has been quantified in Figure 6 and the error introduced has been discussed in Section 4.6.

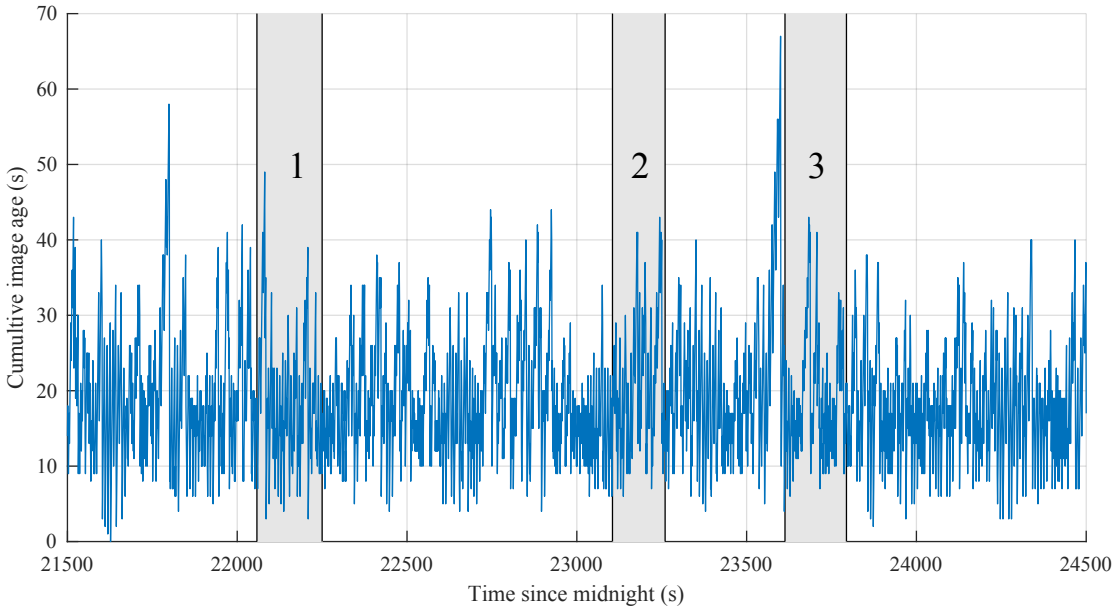

Figure 6: The cumulative age of the quad of images being processed at each interval as the algorithm is applied at regular intervals over the capture duration. As expected, the age varies randomly between 0 and approximately 40s due to each camera having a slightly variable capture interval between 9-11 s. The grey bars show the intervals where significant eruptions occurred and match with with plume volume estimate shown in Figure 9

.

The space carving algorithm requires the manipulation of large sets of 2-D and 3-D data and thus the resolution has a significant impact on computational cost. The maximum voxel resolution can be defined using the known 2-D camera resolutions by projecting the width of a single pixel into the world coordinate system. In this study, the OBS camera was fitted with a 35 mm lens and provided the most detailed view of the summit. Projecting a single pixel width (25 µm) over the 7.6 km range, equates to a 5.7 m voxel size. If an initial search grid is defined to cover the entire sky at this resolution, then the computational requirements quickly exceed that available to most desktop users. Therefore an adaptive search area method was developed.

At each time-step, the algorithm's output is a set of 3-D voxels defining the detected plume. By assuming the plume will occupy a similar region in the following time-step, a new search area is defined as a region encapsulating the current detected region, plus a margin to allow for expansion and drift of the plume. The new search region is defined using the maximum and minimum extent of the plume in each of the three axes. To quantify the increase in efficiency, the algorithm was run for a single eruption sequence lasting 200 s with and without the adaptive search volume process. In both cases it was assumed that the location of the plume was unknown, hence the initial search volume was set large enough to cover the entire sky. Figure 7 compares the cumulative computational times. For an identical 30 m resolution, the adaptive search method reduced the solution time from 46 min to 170 s. Therefore the algorithm could be run in real-time assuming the image capture rate could be increased to 1 Hz.

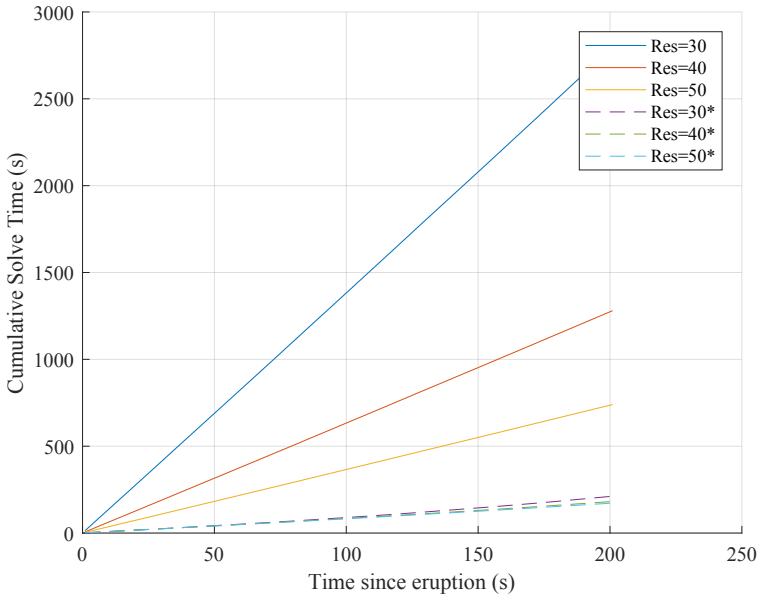

Figure 7: A comparison of the total cumulative solve time for a 200 s sequence. For Res=30, Res=40, Res=50 (solid lines), the search area was set to cover the entire region within view of the cameras and remained constant throughout the sequence, and the value represents the voxel resolution. For the dashed lines, the adaptive search region was active and resulted in significantly shorter solution times.

4.6. Limitations and Sources of Error

The system described is intended to provide a proof of principle for reconstruction of ash plumes using a small number of ground based cameras situated around the base of the volcano. The focus has been on establishing whether such a system is feasible and to demonstrate its practical use in a realistic setting. However, it should be noted that there are limitations with the method adopted and also several sources of error in the system as described, which will impact on the quality of the plume reconstruction.

Space carving has limitations in terms of accurately determining the 3-D reconstruction of the ash plume, especially when using a small number of cameras. As illustrated in Figure 8(a), errors result when there are concavities and voids in the plume (carving 'fills' these as it estimates the 'photo hull' - the largest possible 3-D reconstruction consistent with the images [43]) leading to an overestimation of volume. The quantitative analysis of such errors will be specific to the plume shape which itself is dependent upon volcanic and metrological conditions, hence would require a larger data set from both Fuego and other volcanoes to understand the statistical significance. Errors will also occur from quantisation of the 3-D space due to image resolution as discussed earlier and from the limited number and configuration of the cameras, which also leads to over estimation of the plume volume. The latter is especially relevant when using ground based cameras since the upper surface of the plume is not visible. Errors will also occur from inaccuracies of the camera orientation estimates, due for example to errors in the DEM and estimation of the volcano outline, and the position estimates resulting from GPS errors. Of these, the orientation errors have most impact, due to the distance of the volcano from the cameras, although it is worth noting that orientation errors will have the

effect of under estimating the plume volume, assuming the errors are uncorrelated. Difficulties with problematic plume shapes could be resolved by using more cameras with a greater variation in viewpoints, for example imagery from satellites or drones. Other improvements could including measurements from other sensors such as UV cameras [13] or scanning differential optical absorption spectroscopy (DOAS) [47].

Synchronisation of the cameras is also a critical factor in determining a consistent reconstruction. Time misalignment of frames from the cameras will result in the plume being under and over estimated along its direction of travel as shown in Figure 8(b). To limit this form of error in this study the image sequences were aligned manually by eye, based on the start time of the eruptions since the initial plume was visible in all four cameras. An assessment of Figure 6 shows the camera capture timings for this experiment are sub-optimal with almost no time when all four cameras captured simultaneously. Future work will look at defining a more robust automated process for synchronisation and quantitative analysis of the impact of the sources of error on 3-D reconstruction accuracy.

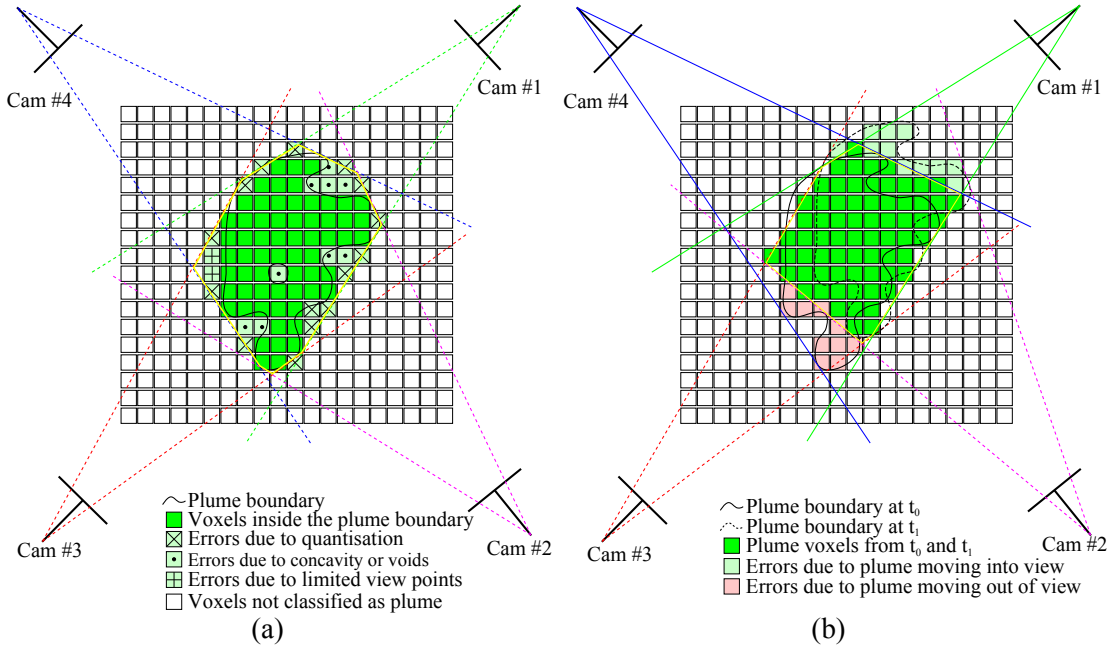

Figure 8: Space carving errors: (a) over estimation of plume volume due to quantisation of 3-D space, the presence of concavities and voids in the plume and the limited number and configuration of the ground cameras; (b) under and over estimate of plume volume along the direction of plume travel due to time-misalignment of images from ground cameras.

5. Results and Discussion

The plume reconstruction algorithm was applied continuously to the entire Fuego data set with a $t_s = 1$s and $\delta_v = 25$m. The timings are measured in seconds since midnight on the morning of 2017-11-06 UTC, therefore the start time was set as $t_0 = 21500$s and the final time as $t_1 = 24500$s for a total of 3001 processed time-steps. During this period all four cameras were operating and the three eruptions occurred. The quantity of detected plume pixels has been calculated for each time step and is shown in Figure 9. The three eruptions can clearly be identified by the rapid increases in volume against the near zero volume detected during periods

of background degassing. For this example, by applying a threshold criteria to the number of plume voxels, it would be possible to automatically determine the eruption times, without manual human assessment. However, as noted previously, the presence of meteorological cloud confounds the 3-D retrieval, and the technique, whilst it could be fully automated in principle, would need to be modified to account for this if continuous monitoring without human intervention was required.

For each eruption, the number of detected voxels initially increases due to the natural expansion of the plume. The volume then peaks before decreasing. This is due to the plume diluting below the 2-D segmentation threshold (see Section 4.4) and also because the plume drifts beyond the view of the cameras. The most accurate detection period is when the plume is within the view of all cameras. This period has been marked on Figure 9 by the grey boxes.

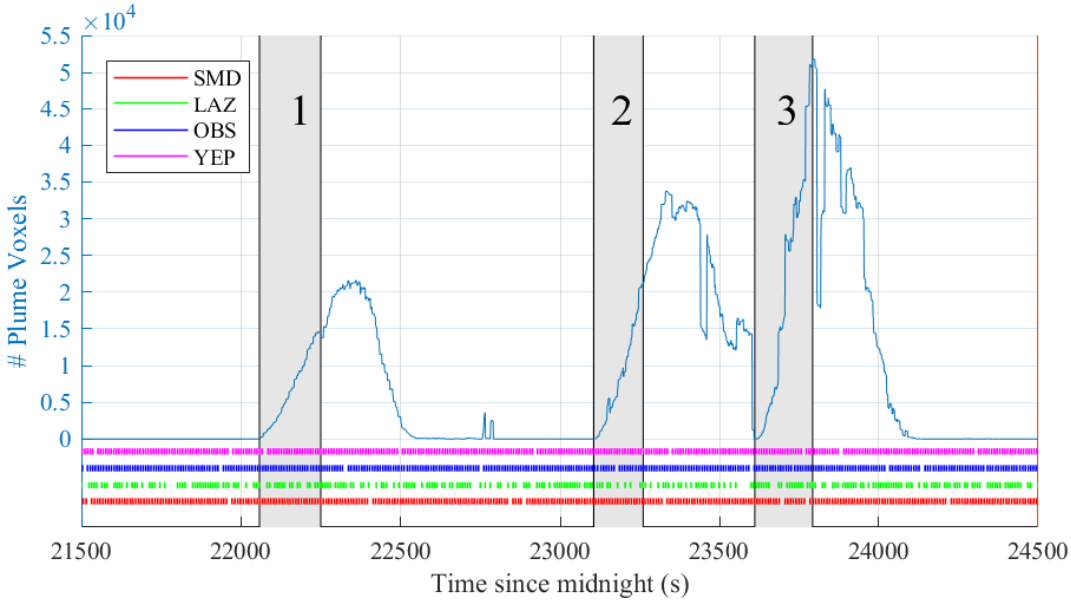

Figure 9: The timings of the data set and results. The times are expressed as seconds past midnight on the morning of 2017-11-06 UTC. The cameras were set to their maximum capture rate with approximately $8-9$s intervals between broadband images. There are slight variations in the rate due to operating system interruptions to the camera control software. The blue line is quantity of plume voxels identified. The coloured markers show the timings of broadband image captures. The grey boxes show the duration of the three eruptions from when a volume is first detected, until the plume leaves the 2-D image bounds of at least one camera.

The set of plume voxels can also be imported into an animation package to produce 3-D visualisations of the eruptions relative to the DEM model. A selection of such renderings are shown in Figure 10.

Since each voxel is defined by its centre point ($\mathbf{V}$), the results can also be thought of as a point cloud and further analysed for a number of higher level physical properties. For example, the total volume, plume height, horizontal drift speed, drift heading can all be calculated. These properties represent the advantages of using a 3-D reconstruction since they cannot be measured from a single 2-D image without assumptions of plume shape.

Volume. The plume volume can be estimated by multiplying the quantity of voxels with the voxel volume. Each voxel has a volume of δ_v^3, hence in this example

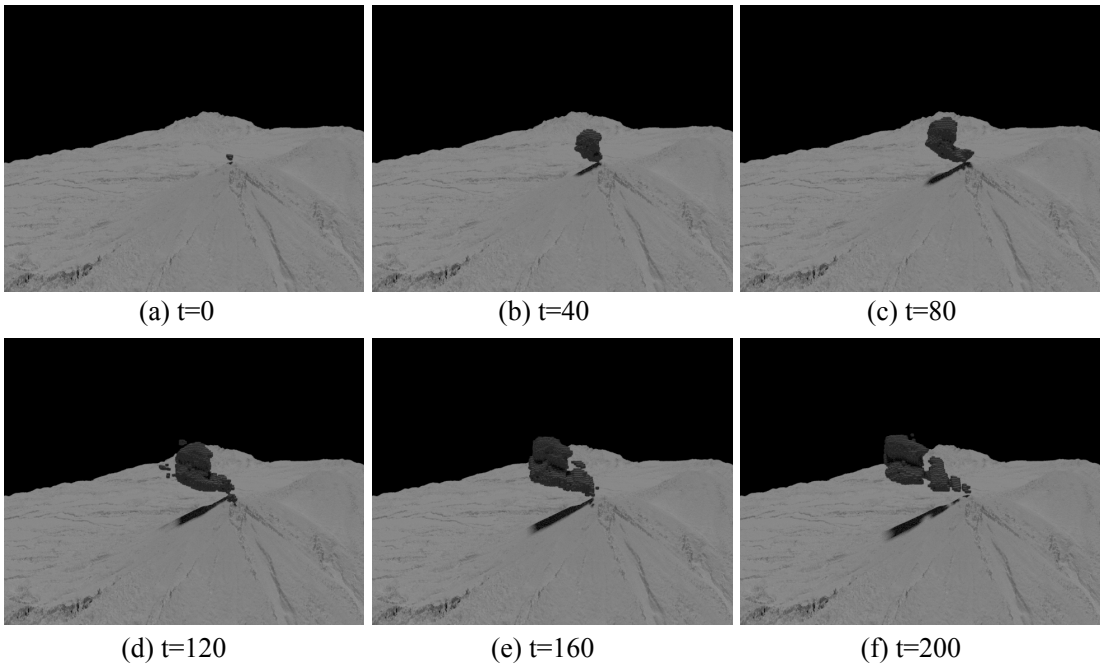

Figure 10: A 3-D visualisation of the plume after an eruption. The time is relative to the moment when the eruption was first detected.

15 625 m^3 per voxel. The volume has been calculated for each of the three eruptions and is shown on Figure 11(a).

Height. The plume cloud top height can be identified by looking for the voxel with the greatest altitude above the summit. Figure 11(b) shows the evolution of the plume height for the eruptions. In each case the behaviour appears asymptotic. For small plumes such as this, that asymptote is approximately the height of neutral buoyancy, whereas for larger plumes significant convective overshoot is possible.

Speed. The drift speed can be measured by identifying the voxel with the greatest separation from the summit. By evaluating the norm of the North/East location of each voxel, the planar distance to the summit can be found. The time-progression of the furthest point is shown in Figure 11(c). Although there are some irregularities near the start of each eruption, the behaviour settles to a linear trend, suggesting the plume has reached a terminal velocity when being carried by the wind. A lower bound of the wind speed can be estimated by considering the linear gradient. For the first eruption this is approximately 10 $m\,s^{-1}$.

Heading. The centroid of the point cloud represents the mean motion of the plume. By considering the direction of the centroid, the plume drift direction can be determined. The motion of the centroid has been plotted onto a satellite view of the summit region in Figure 11(d). The plume will predominately move in the direction of the prevailing winds, however, the 3-D reconstruction allows for a more accurate measurement of the plume location taking into account any local topographical influences, or rapidly changing wind conditions.

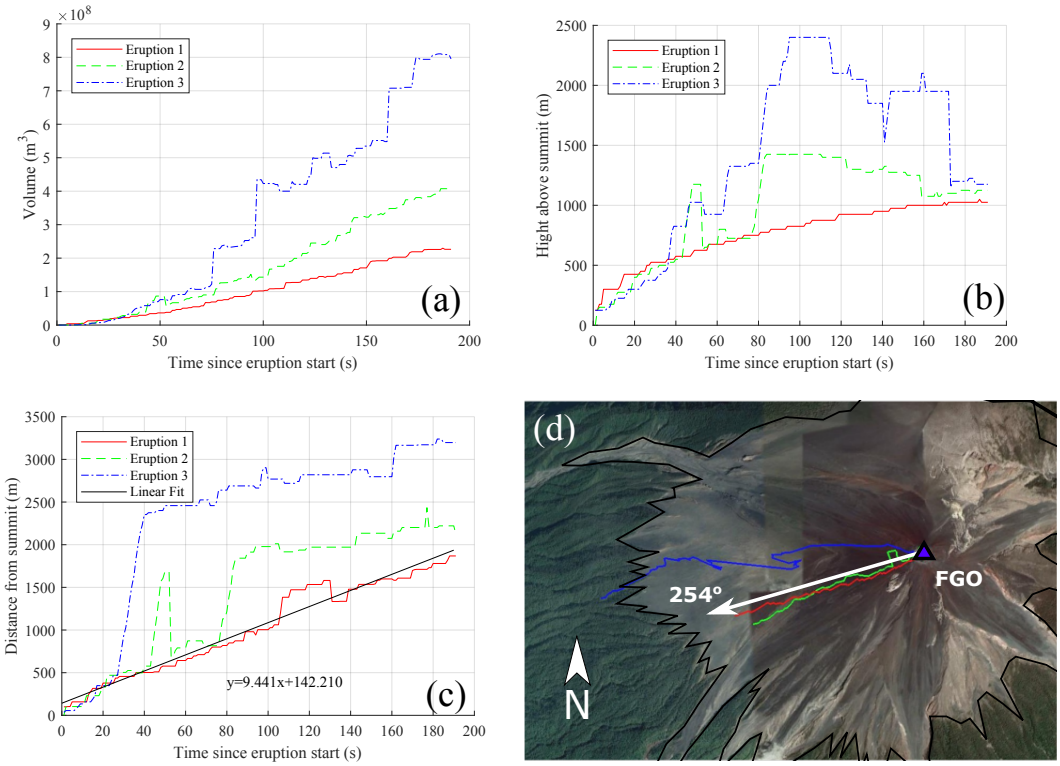

Figure 11: Various quantitative metrics extracted from the space carving method. (a) The calculated volume *vs* time. (b) the calculated highest point in the plume *vs* time. (c) the furthest voxel from the summit *vs* time. (d) The location of the furthest point in the plume overlayed onto a satellite image of the area.

6. Conclusions and Further Work

In this study we have shown that the time-varying spatial properties of a volcanic plume can be directly measured using infra-red images captured from multiple viewpoints. The complete method workflow has been presented from data capture through to the processing of quantitative results. At its core, the process uses a space carving method to discretely identify the plume volume resulting in a point-cloud of voxels. Although space-carving has been previously documented, this is the first application of such a method to volcanic plume measurements. This method is suited to this application due to the large distances and low definition of the thermal images. A novel method was developed for optimising the camera orientations based upon an accurate terrain model of the area.

The set of derived voxels have been analysed to provide direct measurements of the plume physical properties such as volume, height, drift speed, and heading. These properties can be directly measured in 3-D rather than relying upon approximations or assumptions of the plume structure which are often applied to 2-D analyses. This method could also have a direct application for volcano monitoring since multi-angle observations of volcanic plumes can also provide a method of automatically collecting quantitative statistical data, such as counting the number of eruptions and comparing their magnitudes. If the cameras can be permanently installed and the images transmitted live, the plume height and heading data could also be directly used by the local air-space coordinators to inform decisions about

route warnings or closures.

The method was applied to an example data set collected at Volcán de Fuego, Guatemala where four cameras were used. Although quantitative data has been produced, this paper has focused more on the method rather than the geophysical implications. Current 2-D retrievals measure the integral concentration-path length and these are typically combined with estimations of plume speed to retrieve emission rates. Concentration and path length cannot be separated when considering a single viewpoint. However, the 3-D results presented here could be analysed to calculate the path length per pixel, and therefore be used in a future process to normalise the images into concentration maps.

This work represents the first step towards a fully three dimensional retrieval of ash mass and gas concentrations. For an ash concentration map to be estimated, an assumption must be made about the particle size distribution. This could be based upon a direct measurement (for example using unmanned aerial vehicles), or using the methods developed from 2D image analysis [14]. This would provide a step-change in our ability to monitor volcanic emissions and more effectively manage airspace.

Acknowledgements

We would like to thank C. Bernardo, F. Prata and J. Forster for their assistance with set-up for the deployment and automation of the software. Thanks also to G. Chigna and INSIVUMEH, the La Reunion Golf Resort and M. Purvis from Geo Travel Guatemala. This research was funded by the University of Bristol Strategic Research Fund and the Cabot Institute. HET was partly funded by NERC grant number NE/P006744/1. KS was funded by the European Research Council (ERC) under the European Union Horizon 2020 research and innovation program under grant agreement No 670462 (COMTESSA).

References

[1] A. Aiuppa, R. Moretti, C. Federico, G. Giudice, S. Gurrieri, M. Liuzzo, P. Papale, H. Shinohara, M. Valenza, Forecasting Etna eruptions by real-time observation of volcanic gas composition, Geology 35 (12) (2007) 1115–1118. doi:10.1130/G24149A.1.

[2] P. Delmelle, Environmental impacts of tropospheric volcanic gas plumes, Geological Society, London, Special Publications 213 (1) (2003) 381–399. doi:10.1144/GSL.SP.2003.213.01.23.

[3] P. J. Baxter, C. J. Horwell, The Encyclopedia of Volcanoes (Second Edition), Elsevier, 2015, Ch. Chapter 60 - Impacts of Eruptions on Human Health, pp. 1035–1047. doi:10.1016/B978-0-12-385938-9.00060-2.

[4] M. Guffanti, T. J. Casadevall, K. Budding, Encounters of aircraft with volcanic ash clouds - a compilation of known incidents, 1953 - 2009, Tech. rep., U.S. Geological Survey Data Series 545 (2010).

[5] C. Christmann, R. R. Nunes, A. R. Schmitt, Recent encounters of aircraft with volcanic ash clouds, in: Deutscher Luft- und Raumfahrtkongress, 2015.

[6] H. E. Thomas, I. M. Watson, Observations of volcanic emissions from space: current and future perspectives, Natural Hazards 54 (2) (2010) 323–354. doi:10.1007/s11069-009-9471-3.

[7] S. Wen, W. I. Rose, Retrieval of sizes and total masses of particles in volcanic clouds using AVHRR bands 4 and 5, Journal of Geophysical Research - Atmospheres 99 (D3) (1994) 5421–5431. doi:10.1029/93JD03340.

[8] K. L. Wilkins, I. M. Watson, N. I. Kristiansen, H. N. Webster, D. J. Thomson, H. F. Dacre, A. J. Prata, Using data insertion with the NAME model to simulate the 8 May 2010 Eyjafjallajökull volcanic ash cloud, Journal of Geophysical Research - Atmospheres 121 (1) (2016) 306–323. doi:10.1002/2015JD023895.

[9] K. L. Wilkins, L. M. WesternaI, M. Watson, Simulating atmospheric transport of the 2011 grímsvötn ash cloud using a data insertion update scheme, Atmospheric Environment 141 (2016) 48–59. doi:10.1016/j.atmosenv.2016.06.045.

[10] S. Mackie, S. Millington, I. M. Watson, How assumed composition affects the interpretation of satellite observations of volcanic ash, Meteorological Applications 21 (1) (2014) 20–29. doi:10.1002/met.1445.

[11] L. Mastin, M. Guffanti, R. Servranckx, P. Webley, S. Barsotti, K. Dean, A. Durant, J. Ewert, A. Neri, W. Rose, D. Schneider, L. Siebert, B. Stunder, G. Swanson, A. Tupper, A. Volentik, C. Waythomas, A multidisciplinary effort to assign realistic source parameters to models of volcanic ash-cloud transport and dispersion during eruptions, Journal of Volcanology and Geothermal Research 186 (1-2) (2009) 10–21. doi:10.1016/j.jvolgeores.2009.01.008.

[12] F. M. Beckett, C. S. Witham, M. C. Hort, J. A. Stevenson, C. Bonadonna, S. C. Millington, The sensitivity of NAME forecasts of the transport of volcanic ash clouds to the physical characteristics assigned to the particles, Tech. rep., Met Office Forecasting Research Technical Report No. 592 (2014).

[13] G. Bluth, J. Shannon, I. Watson, A. Prata, V. Realmuto, Development of an ultra-violet digital camera for volcanic SO_2 imaging, Journal of Volcanology and Geothermal Research 161 (1-2) (2007) 47–56. doi:10.1016/j.jvolgeores.2006.11.004.

[14] T. Lopez, H. Thomas, A. Prata, A. Amigo, D. Fee, D. Moriano, Volcanic plume characteristics determined using an infrared imaging camera, Journal of Volcanology and Geothermal Research 300 (2015) 148–166. doi:10.1016/j.jvolgeores.2014.12.009.

[15] A. McGonigle, T. Pering, T. Wilkes, G. Tamburello, R. D'Aleo, M. Bitetto, A. Aiuppa, J. Willmott, Ultraviolet imaging of volcanic plumes: A new paradigm in volcanology, Geosciences 7 (3) (2017) 68. doi:10.3390/geosciences7030068.

[16] A. Stohl, A. J. Prata, S. Eckhardt, L. Clarisse, A. Durant, S. Henne, N. I. Kristiansen, A. Minikin, U. Schumann, P. Seibert, K. Stebel, H. E. Thomas,

T. Thorsteinsson, K. Tørseth, B. Weinzierl, Determination of time- and height-resolved volcanic ash emissions and their use for quantitative ash dispersion modeling: the 2010 Eyjafjallajökull eruption, Atmospheric Chemistry and Physics 11 (9) (2011) 4333–4351. doi:10.5194/acp-11-4333-2011.

[17] R. J. Clarkson, E. J. Majewicz, P. Mack, A re-evaluation of the 2010 quantitative understanding of the effects volcanic ash has on gas turbine engines, Proceedings of the Institution of Mechanical Engineers, Part G: Journal of Aerospace Engineering 230 (12) (2016) 2274–2291. doi:10.1177/0954410015623372.

[18] A. J. Prata, F. Dezitter, I. Davies, K. Weber, M. Birnfeld, D. Moriano, C. Bernardo, A. Vogel, G. S. Prata, T. A. Mather, H. E. Thomas, J. Cammas, M. Weber, Artificial cloud test confirms volcanic ash detection using infrared spectral imaging, Scientific Reports 6 (2016) 25620. doi:10.1038/srep25620.

[19] A. Prata, N. Kristiansen, H. Thomas, A. Stohl, Ash metrics for European and trans-Atlantic air routes during the Eyjafjallajökull eruption 14 april - 23 may, Journal of Geophysical Research: Atmospheres 123 (10) (2018) 5469–5483. doi:10.1002/2017JD028199.

[20] A. Prata, C. Bernardo, Retrieval of volcanic ash particle size, mass and optical depth from a ground-based thermal infrared camera, Journal of Volcanology and Geothermal Research 186 (1-2) (2009) 91–107. doi:10.1016/j.jvolgeores.2009.02.007.

[21] A. J. Prata, C. Bernardo, Retrieval of sulfur dioxide from a ground-based thermal infrared imaging camera, Atmospheric Measurement Techniques 7 (9) (2014) 2807–2828. doi:10.5194/amt-7-2807-2014.

[22] H. Thomas, A. Prata, Computer vision for improved estimates of SO_2 emission rates and plume dynamics, International Journal of Remote Sensing 39 (5) (2018) 1285–1305. doi:10.1080/01431161.2017.1401250.

[23] E. Frins, N. Bobrowski, M. Osorio, N. Casaballe, G. Belsterli, T. Wagner, U. Platt, Scanning and mobile multi-axis DOAS measurements of SO_2 and NO_2 emissions from an electric power plant in Montevideo, Uruguay, Atmospheric Environment 98 (2014) 347–356. doi:10.1016/j.atmosenv.2014.03.069.

[24] M. Osorio, N. Casaballe, G. Belsterli, M. Barreto, A. Gomez, C.mez, J. A. Ferrari, E. Frins, Plume segmentation from UV camera images for SO_2 emission rate quantification on cloud days, Remote Sensing 9 (6). doi:10.3390/rs9060517.

[25] U. Platt, P. Lübcke, J. Kuhn, N. Bobrowski, F. Prata, M. Burton, C. Kern, Quantitative imaging of volcanic plumes - results, needs, and future trends, Journal of Volcanology and Geothermal Research 300 (2015) 7–21. doi:10.1016/j.jvolgeores.2014.10.006.

[26] U. Platt, N. Bobrowski, A. Butz, Ground-based remote sensing and imaging of volcanic gases and quantitative determination of multi-species emission fluxes, Geosciences 8 (2). doi:10.3390/geosciences8020044.

[27] K. Zaksek, M. R. James, M. Hort, T. Nogueira, K. Schilling, Using picosatellites for 4-D imaging of volcanic clouds: Proof of concept using ISS photography of the 2009 Sarychev Peak eruption, Remote Sensing of Environment 210 (2018) 519–530. doi:10.1016/j.rse.2018.02.061.

[28] J. Gliß, K. Stebel, A. Kylling, A. Sudbø, Improved optical flow velocity analysis in SO_2 camera images of volcanic plumes – implications for emission-rate retrievals investigated at Mt Etna, Italy and Guallatiri, Chile, Atmospheric Measurement Techniques 11 (2) (2018) 781–801. doi:10.5194/amt-11-781-2018.

[29] M. Bombrun, D. Jessop, A. Harris, V. Barrab, An algorithm for the detection and characterisation of volcanic plumes using thermal camera imagery, Journal of Volcanology and Geothermal Research 352 (2018) 26–37. doi:10.1016/j.jvolgeores.2018.01.006.

[30] S. Valadea, A. Harris, M. Cerminara, Plume Ascent Tracker: Interactive Matlab software for analysis of ascending plumes in image data, Computers & Geosciences 66 (2014) 132–144. doi:10.1016/j.cageo.2013.12.015.

[31] C. Gomez, B. Kennedy, Capturing volcanic plumes in 3D with UAV-based photogrammetry at Yasur Volcano - Vanuatu, Journal of Volcanology and Geothermal Research 350 (2017) 84–88. doi:10.1016/j.jvolgeores.2017.12.007.

[32] G. T. Herman, Fundamentals of Computerized Tomography, Springer, 2009. doi:10.1007/978-1-84628-723-7.

[33] K. J. Batenburg, J. Sijbers, DART: A practical reconstruction algorithm for discrete tomography, IEEE Transactions on Image Processing 20 (9) (2011) 2542–2553. doi:10.1109/TIP.2011.2131661.

[34] R. Kazahaya, T. Mori, K. Kazahaya, J. ichi Hirabayashi, Computed tomography reconstruction of SO_2 concentration distribution in the volcanic plume of Miyakejima, Japan, by airborne traverse technique using three UV spectrometers, Geophysical Research Letters 35 (13). doi:10.1029/2008GL034177.

[35] M. Cerminara, T. E. Ongaro, S. Valade, A. J. Harris, Volcanic plume vent conditions retrieved from infrared images - A forward and inverse modeling approach, Journal of Volcanology and Geothermal Research 300 (2015) 129–147. doi:10.1016/j.jvolgeores.2014.12.015.

[36] A. Jordt, C. Zelenka, J. S. von Deimling, R. Koch, K. Köser, The Bubble Box: Towards an automated visual sensor for 3D analysis and characterization of marine gas release sites, Sensors 15 (12) (2015) 30716–30735. doi:10.3390/s151229825.

[37] C. Beekmans, J. Schneider, T. Läbe, M. Lennefer, C. Stachniss, C. Simmer, Cloud photogrammetry with dense stereo for fisheye cameras, Atmospheric Chemistry and Physics 16 (2016) 14231–14248. doi:10.5194/acp-16-14231-2016.

[38] Z. Peng, D. Yu, D. Huang, J. Heiser, S. Yoo, P. Kalb, 3D cloud detection and tracking system for solar forecast using multiple sky imagers, Solar Energy 118 (2015) 496–519. doi:10.1016/j.solener.2015.05.037.

[39] P. Rusch, R. Harig, 3-D reconstruction of gas clouds by scanning imaging IR spectroscopy and tomography, IEEE Sensors 10 (3). doi:10.1109/JSEN.2009.2038450.

[40] L. A. Rodriguez, I. M. Watson, W. I. Rose, Y. K. Branan, G. J. Bluth, G. Chigna, O. Matias, D. Escobar, S. A. Carn, T. P. Fischer, SO_2 emissions to the atmosphere from active volcanoes in Guatemala and El Salvador, 1999 - 2002, Journal of Volcanology and Geothermal Research 138 (3-4) (2004) 325–344. doi:10.1016/j.jvolgeores.2004.07.008.

[41] P. A. Nadeau, J. L. Palma, G. P. Waite, Linking volcanic tremor, degassing, and eruption dynamics via SO_2 imaging, Geophysical Research Letters 38 (1) (2011) L01304. doi:10.1029/2010GL045820.

[42] G. Cai, B. M. Chen, T. H. Lee, Unmanned Rotorcraft Systems, Springer-Verlag London, 2011. doi:10.1007/978-0-85729-635-1.

[43] K. Kutulakos, S. Seitz, A theory of shape by space carving, International Journal of Computer Vision 38 (3) (2000) 199–218. doi:10.1023/A:1008191222954.

[44] T. Luhmann, S. Robson, S. Kyle, J. Boehm, Close-Range Photogrammetry and 3D Imaging (2nd Edition), De Gruyter, 2013. doi:10.1111/phor.12056.

[45] Z. Zhang, A flexible new technique for camera calibration, IEEE Transactions on Pattern Analysis and Machine Intelligence 22 (11) (2000) 1330–1334. doi:10.1109/34.888718.

[46] Global positioning system standard positioning service performance standard, Tech. rep., U.S. Department of Defense (2008).

[47] A. McGonigle, C. Oppenheimer, B. Galle, T. Mather, D. Pyle, Walking traverse and scanning doas measurements of volcanic gas emission rates, Geophysical Research Letters 29 (20). doi:10.1029/2002GL015827.

Appendix A. Thermal Camera Intrinsic Calibration

The thermal camera intrinsic properties can be found in the equipment data sheets, however unless perfectly manufactured there will be subtle differences between the idealised system and the real world system.

It is possible to estimate the intrinsic and lens properties using camera calibration techniques. There are several available, and most expect a series of images of a regular grid as an input. The process described here is based on the method described by [45]. The method requires capturing a set of images of a chequerboard target and has been implemented as part of the Computer Vision toolbox in MATLAB 2016a. To maximise the accuracy, the images should a) be captured from many orientations, b) capture the entire target, and c) use the same focus as in the field tests. For the latter requirement, the cameras were effectively focused at infinity distance.

For normal visible light cameras, the black and white chequerboard can be printed on allowing the user to quickly capture images by hand in a desktop environment. The use of thermal cameras, however, presented additional challenges.

To a thermal camera, a printed target would appear plain, since the black and white squares would be at the same temperature. Also, since the cameras were used for imaging a plume at between 8 – 12 kilometres they were essentially focused at infinity range. A printed paper target would occupy a small region of the image when placed at sufficient distance to be in focus. To address these issues a custom thermal target was created.

The thermal target was created by painting a matt black chequerboard pattern onto a sheet of polished aluminium as shown in Figure A.12(a). The painted squares have a higher emissivity while the unpainted squares reflect light from other parts of the room. By heating the metal target in a cold room, the black squares appeared hotter and were distinctly visible in the IR images as shown in Figure A.12(b). The overall dimensions of the sheet were 1.25 m × 1.25 m with each square having sides of 125 mm length.

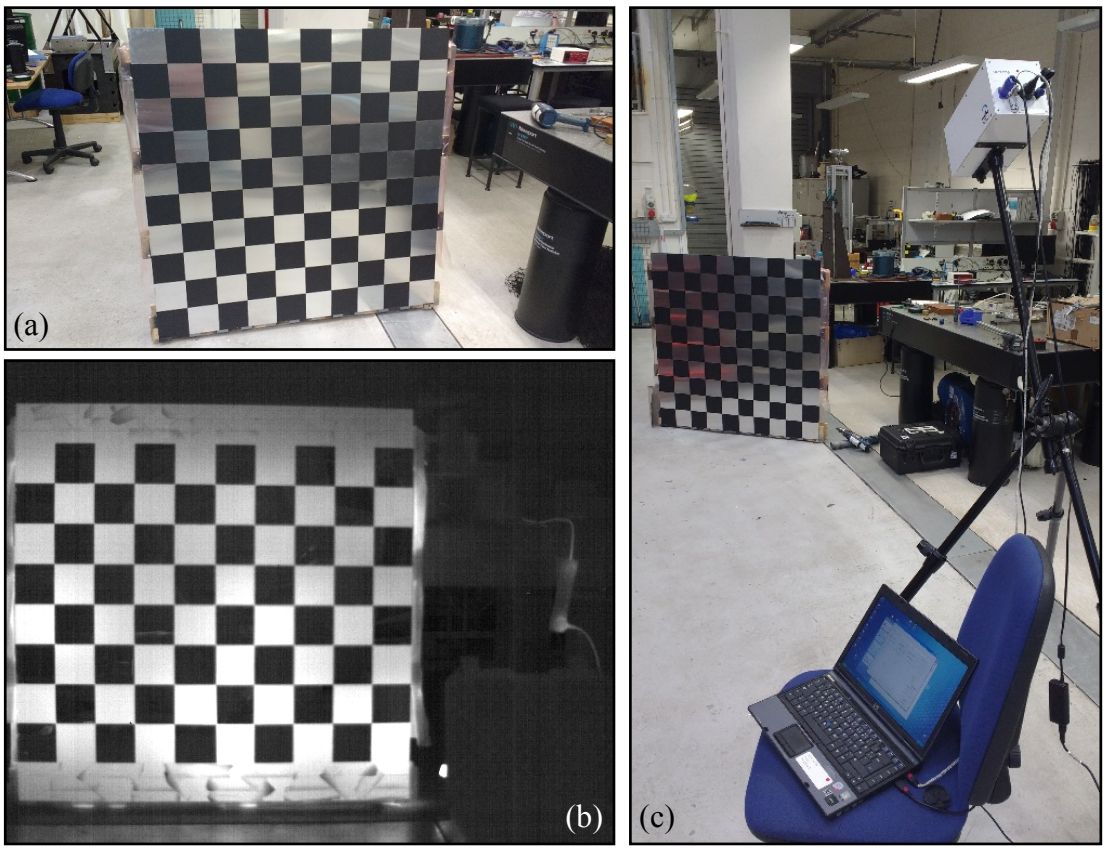

Figure A.12: Camera calibration: (a) thermal calibration target manufactured by painting black squares onto an aluminium sheet; (b) example calibration image captured by the thermal camera (note the visibility of the pattern); (c) thermal camera and control laptop, with camera-target separation of approximately 5 m, which was sufficient for the target to appear in focus.

Not all of the cameras used in the Guatemala study were available for calibration. However, one camera with a 25 mm lens and one with a 35 mm lens were available for calibration using the thermal target. The values for the focal lengths, principal point, and lens parameters are given in Table A.2. As a sanity check, the measured focal lengths were consistent with the manufacturers data sheet, although the measured values are slightly lower. For each lens and filter combination the principal point was within ±10px of the ideal image centre ([322,256]).

Table A.2: The optical properties as a result of the camera calibration process using N images and filters (F) 1-4 and mean pixel error (e) following calibration. Only two cameras were available for calibration, one with a 25 mm lens and one with a 35 mm lens.

Camera	F	N	f_x mm	f_y mm	c_x	c_y	k_1	k_2	e
SMD	1	28	24.93	24.93	330.57	255.29	-0.2073	0.0062	0.3442
SMD	2	26	24.93	24.93	330.42	259.91	-0.2001	0.0216	0.3441
SMD	3	27	24.94	24.94	329.92	256.71	-0.1962	-0.0280	0.3453
SMD	4	26	24.91	24.91	329.23	254.60	-0.1811	-0.0977	0.3515
OBS	1	58	34.75	34.73	332.06	264.77	0.1676	-0.3109	0.3049
OBS	2	61	34.70	34.68	332.81	259.68	0.1639	0.0119	0.3156
OBS	3	58	34.75	34.73	331.80	263.59	0.1730	-0.3697	0.3045
OBS	4	52	34.80	34.77	332.99	262.90	0.1693	-0.1257	0.3288

Appendix B. Curved-Earth Coordination Transformation

The following describes the exact transformation between latitude (φ_p), longitude (λ_p), altitude (h_p) location (subscript p) expressed relative to the WGS84 ellipsoid, and a right-hand orthogonal Cartesian location relative to a defined referent point (subscript r) with a plane tangential to the Earth's surface. The reference location is also in the WGS84 system (φ_r,λ_r,h_r).

Initially, both the location of interest and the reference location are transformed into an orthogonal Cartesian coordinate system referenced to the centre of the Earth, commonly known as the Earth Centred Earth Fixed (ECEF) system.

$$T_{p,r} = \begin{pmatrix} X_{p,r} \\ Y_{p,r} \\ Z_{p,r} \end{pmatrix} = \begin{pmatrix} (N_e + h_{p,r}) \cos\varphi_{p,r} \cos\lambda_{p,r} \\ (N_e + h_{p,r}) \cos\varphi_{p,r} \sin\lambda_{p,r} \\ (N_e\,(1 - e^2) + h_{p,r}) \sin\varphi_{p,r} \end{pmatrix} \tag{B.1}$$

where,

$$e^2 = 2f - f^2 \tag{B.2}$$

$$N_e = \frac{a}{\sqrt{1 - e^2 \sin^2 \varphi_{p,r}}} \tag{B.3}$$

This is an exact transformation and results in very large values describing locations within a system encompassing the entire planet. A second process is then applied to express locations in a local North, East, Down (NED) relative to the reference location. This comprises two steps: (1) find relative vector between a given point (T_p) to a reference point (T_r), (2) rotate the vector using the local surface orientation.

$$T = R\,(T_p - T_r) \tag{B.4}$$

where R is a rotation matrix created using two successive rotations about orthogonal

axes using the geodetic longitude and latitude at the reference location.

$$R = \begin{bmatrix} -\sin\varphi_r \cos\lambda_r & -\sin\varphi_r \sin\lambda_r & \cos\varphi_r \\ -\sin\lambda_r & \cos\lambda_r & 0 \\ -\cos\varphi_r \cos\lambda_r & -\cos\varphi_r \sin\lambda_r & -\sin\varphi_r \end{bmatrix} \tag{B.5}$$